

# **REMOTE RAMAN DETECTION OF NATURAL ROCKS**

A FINAL REPORT SUBMITTED TO THE DEPARTMENT OF  
GEOLOGY AND GEOPHYSICS, UNIVERSITY OF HAWAI'I  
AT MĀNOA, IN PARTIAL FULFILLMENT OF THE  
REQUIREMENTS FOR THE DEGREE OF

## **MASTER OF SCIENCE IN GEOLOGY AND GEOPHYSICS**

August 2017

By  
Genesis Berlanga

Advisor:  
Dr. Anupam K. Misra

# Remote Raman Detection of Natural Rocks

GENESIS BERLANGA,<sup>1,2\*</sup> TAYRO E. ACOSTA-MAEDA,<sup>1</sup> SHIV K. SHARMA,<sup>1</sup> JOHN N. PORTER,<sup>1</sup> PRZEMYSŁAW DERA,<sup>1</sup> HANNAH SHELTON,<sup>1,2</sup> G. JEFFREY TAYLOR,<sup>1</sup> ANUPAM K. MISRA<sup>1</sup>

<sup>1</sup>Hawai'i Institute of Geophysics and Planetology, University of Hawai'i, POST #602, 1680 East-West Road, Honolulu, Hawaii 96822, USA

<sup>2</sup>Department of Geology and Geophysics, University of Hawai'i, POST #702, 1680 East-West Road, Honolulu, Hawaii 96822, USA

\*Corresponding author: [genesis.berlanga@gmail.com](mailto:genesis.berlanga@gmail.com)

Received XX Month XXXX; revised XX Month, XXXX; accepted XX Month XXXX; posted XX Month XXXX (Doc. ID XXXXX); published XX Month XXXX

**We report remote Raman spectra of natural igneous, metamorphic, and sedimentary rock samples at a standoff distance of 5 m. High quality remote Raman spectra of unprepared rocks are necessary for accurate and realistic analysis of future Raman measurements on planetary surfaces such as Mars. Our results display the ability of a portable Compact Remote Raman+LIBS+Fluorescence System (CRRLFS) to effectively detect and isolate various light and dark-colored mineral phases in natural rocks. The CRRLFS easily detected plagioclase and potassium feldspar end members, quartz, and calcite in rocks with high fluorescence backgrounds. Intermediate feldspars and quartz, when found in rocks with complex mineralogies, exhibited band shifts and broadening in the 504-510  $\text{cm}^{-1}$  and 600-1200  $\text{cm}^{-1}$  regions. A good approximation of intermediate plagioclase feldspars was possible by using spectral shape and assigning other minor Raman peaks in addition to the 504-510  $\text{cm}^{-1}$  peaks. Detection of olivine and pyroxene in mafic rocks allowed for compositional characterization.**

**OCIS codes:** (120.0120) Instrumentation, measurement, and metrology; (220.0220) Optical design and fabrication; (280.0280) Remote sensing and sensors; (290.5860) Scattering, Raman; (300.6450) Spectroscopy, Raman; (300.6500) Spectroscopy, time-resolved.

<http://dx.doi.org/10.1364/AO.99.099999>

## 1. INTRODUCTION

Raman spectroscopy is a notable active laser spectroscopy technique that provides molecular and crystal arrangement information about the target material enabling identification of both organics and inorganics. The technique involves shining light from a monochromatic laser, such as a 532 nm laser, on a sample and collecting the resulting scattered light. A fraction of the scattered light is shifted in energy from the laser frequency due to interactions between the incident electromagnetic waves and the vibrational modes of the molecules in the sample. This inelastic shift called the Raman effect occurs effectively instantaneously at picosecond timescales of  $10^{-12}$  s [1], [2]. A Raman spectrum is produced with band positions at frequencies corresponding to the energy levels of different vibrational modes, univocally identifying a target sample [2].

NASA's Mars Science Laboratory (MSL) mission paved the way for active laser spectroscopy on a planetary surface. Curiosity Rover's highly successful ChemCam instrument suite continues to acquire laser-induced breakdown spectroscopy

(LIBS) measurements from standoff distances providing quantitative and qualitative elemental compositions of major and minor minerals on the surface of Mars [3]. This successful laser operation on Mars has opened opportunities for complementary laser based techniques such as remote Raman spectroscopy, to provide additional mineralogical analyses. Raman spectroscopy can identify mineral structure, distinguish between mineral polymorphs such as calcite and aragonite, and the accompanying fluorescence signal can identify biosignatures [4]. A combined approach of using time-resolved Raman along with LIBS and fluorescence spectroscopy in one compact system, as seen in the future Mars 2020 SuperCam instrument, will help in identifying various hydrated and biological minerals which will help in NASA's goal for search of life during planetary surface explorations [4], [5].

With this in mind, it is not surprising that time-resolved remote Raman spectroscopy is increasingly highlighted as a viable method for planetary surface molecular analysis [4], [6]–

[16]. This technique extends traditional micro-Raman techniques to standoff distances of up to hundreds of meters, requires no sample preparation, causes minimal to no sample damage, and can be used under daylight conditions; saving time and increasing the number of accessible targets [7], [17]. The University of Hawai'i (UH) has developed a Compact Remote Raman+LIBS+Fluorescence System (CRRLFS) that is capable of Raman, LIBS, and fluorescence measurements under daytime conditions from standoff distances of several meters [11]. The CRRLFS shown in Figure 1 is one of several in-house remote Raman systems developed for chemical and molecular analysis of liquid, gases, and solids, at distances between 1.5-430 m [18]–[25].

Studies by other laboratory groups have attempted to analyze various pure minerals, powders, and a selection of rocks using standoff and micro-Raman spectroscopy for planetary science applications. Micro-Raman systems use a very small laser spot size in the order of 10  $\mu\text{m}$  in diameter for sample analysis. When studying rocks with multiple minerals, these systems normally give spectra of minerals that fall within the small laser spot size. Hence, it is difficult to identify a rock with a single micro-Raman measurement. To overcome this problem point-counting approaches are employed during which multiple spectra are measured at various parts of the rock to determine the presence of all mineral phases. In remote Raman systems a laser spot size of several millimeters is used and the Raman spectra obtained show the presence of all mineral phases falling within a much larger laser spot size. This technique provides bulk rock mineralogy.

Previous micro-Raman studies have focused on point-counting approaches to accurately characterize bulk rock mineralogies [26]–[29], hand-held Raman studies illustrated the possibility of effective Raman measurements in the field [8], [30], and remote Raman studies using fiber-coupled [4], [9], [22], [23], [31]–[33] and directly coupled optics and spectrograph performed bulk sample analysis with centimeter-sized target areas at standoff distances [34]. Previous studies by the University of Hawai'i at Mānoa Raman research group have demonstrated standoff Raman detection capability for a variety of minerals, rocks, and powder chemicals using fiber-coupled optics and spectrograph [35]. Our directly coupled system design showed significant improvement in remote Raman detection capability over the fiber-coupled system [36]. These directly coupled systems were developed in oblique geometries from 2-50 m [21], [37], and also in coaxial geometries from 1.5-430 m [11], [18]–[20], [24], [25], [36]. The advantages of the coaxial system over the oblique systems are large sampling depth and easy system alignment. Previous work using coaxial systems was mostly focused on obtaining remote Raman spectra of various minerals such as feldspars, hydrated minerals, dark colored minerals, various organic and inorganic chemicals, water, frost, ice, dry ice etc. However, to interpret *in situ* remote Raman measurements from rocks and soils on planetary surfaces such as Mars, standoff Raman measurements of natural, unprepared rock samples are needed. These measurements will be helpful in evaluating future remote

Raman data from Mars using the SuperCam instrument on the Mars2020 mission.

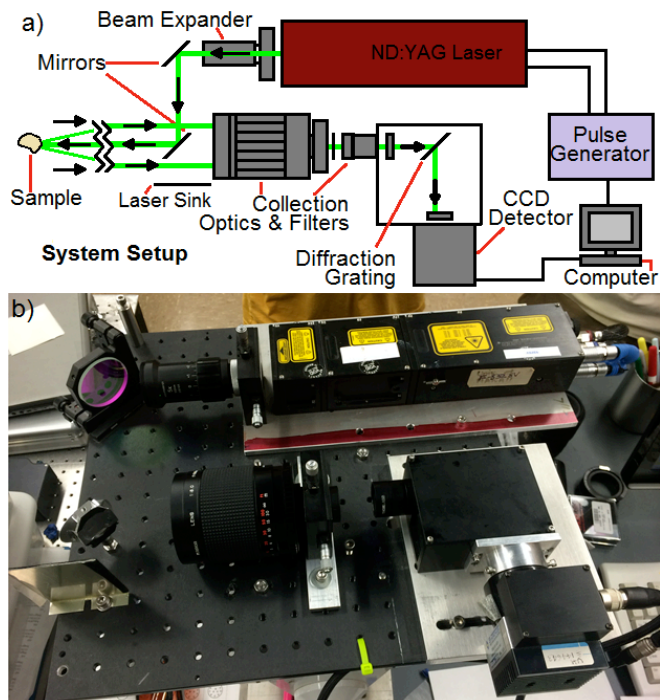


Fig. 1. CRRLFS schematic (above) and actual system (below).

The CRRLFS has been able to successfully acquire high quality Raman spectra of various light and dark minerals, water, water-ice,  $\text{CO}_2$  ice, and organic and inorganic chemicals at distances of up to 50 m with a 10 s integration time [37]. In this study several igneous, sedimentary, and metamorphic rocks were surveyed using the CRRLFS. We report accurate and univocal identification of various mineral phases in natural rock samples using the CRRLFS from a 5 m standoff distance using a 30 s integration time. X-ray diffraction (XRD) analyses were obtained for all samples to establish compositional ground truth for comparison with the standoff Raman spectra.

## 2. METHODOLOGY

### A. Samples

Twenty four rock samples were selected from Ward's Collection of Classic North American Rocks 45-7250, Ward's Rock Forming Mineral Student Set 45 H 0355, and hand samples from the Raman Spectroscopy Laboratory at the University of Hawai'i at Mānoa. Most rocks measured between 2-8 cm in length at their longest dimensions. Alkalic granite (Quincy, MA, USA), nepheline syenite (Bancroft, Ontario, Canada), tonalite (San Diego County, CA, USA), biotite gneiss (Uxbridge, MA, USA), grey sandstone (Berea, OH, USA), red sandstone (Potsdam, NY, USA), quartz conglomerate (Fremont County, CO, USA), quartzite (Baraboo, WI, USA), pyroxenite (harzburgite) (Stillwater Complex, MT, USA), and dunite (olivine peridotite) (Balsam, NC, USA) were chosen due to having more than one mineral component. Pink marble (Tate, GA, USA), dolomite marble (Essex County, NJ, USA), calcite

(unknown locality), and siderite carbonatite (Iron Hill, CO, USA) were chosen due to their systematic chemical differences. Albite (Bancroft, Ontario, Canada), oligoclase (unknown locality), andesine (Keystone, SD, USA), labradorite (unknown locality), bytownite (Crystal Bay, MS, USA), anorthite (Miyakajima, Tokyo, Japan), orthoclase (Gothic, CO, USA), microcline (Madawaska, Ontario, Canada), and milky quartz (Dekalb, NY, USA) were chosen for use as reference minerals to identify individual components in multiminerallitic rocks. These reference minerals include quartz, the entire plagioclase feldspar group, and part of the alkali feldspar group.

Several igneous rocks with varied mineral compositions were analyzed. Nepheline syenite is an igneous intrusive rock composed primarily of nepheline and potassium feldspar. Tonalite (quartz diorite with a quartz content ~20% of the rock) is an igneous intrusive rock containing quartz, biotite, plagioclase feldspars, and orthoclase feldspars. Nepheline reacts with quartz to produce potassium feldspars such as orthoclase. Alkalic granite is an igneous rock generally composed of quartz, potassium feldspars, and minor micas and hornblende. Pyroxenite (harzburgite) is composed primarily of pyroxene, and some minor clinopyroxene or orthopyroxene. Dunitite (olivine peridotite) contains over 90% olivine.

Two metamorphic rocks were studied: Biotite gneiss is a high grade metamorphic rock with banded dark biotite mica and lighter feldspar and quartz. Quartzite is composed of pure quartz sandstone heated and metamorphosed through tectonic orogenic compression. Three sandstones were also measured: Grey sandstone from Berea, OH is historically composed of quartz, feldspar, and organic detritus typical of argillaceous sandstones. Red sandstone from Potsdam, NY is predominantly quartz with accessory hematite impurities. Quartz conglomerate from Fremont County, CO consists of mostly quartz and plagioclase cemented by limestone.

Igneous and clay minerals were used as reference standards for rock component identification. Pink and dolomite marble are primarily composed of calcite the difference being that pink marble has Fe cations and dolomite marble has Mg cations. Siderite is a carbonatite that has iron instead of calcium.

## B. Instrumentation and software

The CRRLFS includes a laser, collection optics, spectrometer, and an intensified charge-coupled device (ICCD) camera. Instrument schematics are shown in Figure 1. The excitation source and collection optics are arranged in a coaxial configuration. The instrument contains a small 532 nm Q-switched frequency-doubled Nd:YAG laser source from BigSky Ultra Lasers operating at 20 Hz (20 mJ/pulse), an adjustable 10x beam expander, a 45°, 532 nm laser mirror from Edmund Optics ( $\lambda/4$  optical flatness), a 7.62 cm diameter mirror lens (Bower) used as a collection telescope (f500 mm at F/8), a Semrock 532 nm long pass filter, a 50  $\mu\text{m}$  slit, a Holoplex stacked volume phase transmission grating from Kaiser Optical Systems, Inc. covering the spectral range from 534-611 nm and 609-696 nm, and a cooled, miniature Syntronics ICCD (1408x1044 pixels). The compact spectrograph is 10 cm long x 8.2 cm wide x 5.2 cm tall. The system is externally triggered

using a BNC Model 575 pulse-delay generator and custom software controls dark image and Raman acquisitions. A good description of the instrument details, gating, and design parameters can be found in Gasda et al. (2015) [11].

Micro-Raman measurements using  $\mu\text{m}$ -sized laser spots require scan and point counting techniques to provide whole rock analysis. By using standoff Raman we benefit from larger size beam diameters (5-10 mm) capable of whole rock analysis that reduce measurement times to seconds and at most minutes. Time-resolved Raman capabilities down to nanosecond timescales have enabled full Raman measurements while eliminating daylight background illumination and minimizing long-lived mineral phosphorescence. By using a directly coupled system design we increase sensitivity by avoiding additional scattering within the fiber optic cable and losses at the optical connections. This combination of system components and architectures allows for a compact system to strike a fine balance between an adequate SNR and fast data acquisition times.

We verified our standoff Raman spectra through micro-Raman spectra using a Renishaw inVia confocal Raman microscope using 514.5 nm laser light. Sample bulk composition was determined through high resolution powder X-ray diffraction (XRD) analysis using a Bruker D8 Advance instrument operating with a copper  $K\alpha$  X-ray source and a Lynx IXE linear array detector. Crystalline phase identification was determined through DiffraC.eva and JADE software packages using a search and match technique with the included Crystallography Open Database (COD). Qualitative Rietveld analysis was conducted using PDIndexer software to determine crystal structures and the chemical composition of the sample mineral components.

## C. Methods

Standoff Raman spectra were acquired for 30 s (600 laser pulses) with a laser spot size of 5 mm and a laser pulse energy of 20 mJ/pulse. The measurements for each target area on a rock were taken three times for verification of system reproducibility. The Raman signal appears as a two trace spectral image on the ICCD upon passing through the slit and diffraction gratings [11]. The two diffraction gratings are stacked and angled slightly differently from each other so that one trace contains the lower frequencies and the other trace contains the higher frequencies. Each trace is vertically binned across all frequencies and the resulting sums (one for each pixel column) are plotted into a spectrum. Spectra were dark subtracted to remove electronic noise. Wavelength calibration was conducted using a neon lamp, sulfur and cyclohexane Raman spectra, and barite LIBS spectra as standards. For the XRD measurements, rock samples were powdered and sieved down to 125  $\mu\text{m}$ . The samples were measured for 15 minutes each while on a flat plate rotating stage. Bruker's DiffraC software processed the XRD image and plotted the spectrum in CPS (counts/s). XRD spectra were dark subtracted, baseline corrected as needed, and  $K\alpha$  lines were removed. The  $2\theta$  values were carefully calibrated using a NIST-supplied (SRM 1976) sintered corundum standard. Micro-Raman

measurements were typically taken with 10 s exposure time and 10 software accumulations with a 50x microscope lens and 2 mW laser power. Micro-Raman spectra were dark subtracted and wavelength calibration was based on Ne emission spectrum and adjusted using a silica wafer standard.

### 3. RESULTS AND DISCUSSION

#### A. Remote Raman Spectra

The CRRLFS is capable of fast data acquisition yielding quality data with high signal to noise ratio. We present remote Raman spectra of several igneous, sedimentary, and metamorphic rocks at 30 s integration times in order to observe the subtler Raman peaks. In most cases, the same peaks are visible at 1 s integration times for the lighter and mixed light and dark sample targets. Darker sample targets required the full 30 s integration time due to the increased mineral opacity and resulting decreased laser penetration.

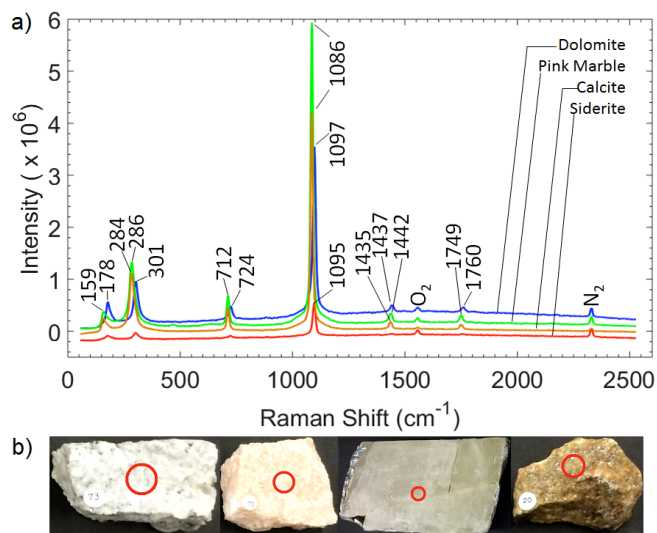


Fig. 2. a) Remote Raman spectra of carbonates at a 5 m distance over a 30 s integration time. Spectra were vertically shifted for viewing clarity. b) Analyzed samples from left to right: dolomite, pink marble, calcite, siderite. Laser target within red circle.

Cation	Mineral (formula)	Observed Raman Peaks (cm <sup>-1</sup> )					
Ca	Calcite (CaCO <sub>3</sub> )	159.4	283.8	712.4	1086	1435	1749
Ca-Fe	Pink Marble (CaFe(CO <sub>3</sub> ) <sub>2</sub> )	159.4	286	712.4	1086	1437	1749
Fe	Siderite (FeCO <sub>3</sub> )	177.7	301.6	724.7	1095	1442	—
Ca Mg	Dolomite Marble (CaMg(CO <sub>3</sub> ) <sub>2</sub> )	177.7	301.6	724.7	1097	1442	1760
	<i>Symmetry</i>	<i>Eg</i>	<i>Eg</i>	<i>Eg</i>	<i>A1g</i>	<i>Eg</i>	<i>Eg</i>

Table 1. Tabulated Raman peaks for Ca, Fe, and Mg bearing carbonates.

Calcite (CaCO<sub>3</sub>), pink marble (CaFe(CO<sub>3</sub>)<sub>2</sub>), siderite carbonatite (FeCO<sub>3</sub> carbonate with a Mg:Fe ratio of ~0.25), and dolomite marble (CaMg(CO<sub>3</sub>)<sub>2</sub>) were analyzed at a 5 m distance over 30 s integration times. They each displayed

strong carbonate Raman peaks at 1085.95, 1086.01, 1095.45, and 1097.34 cm<sup>-1</sup>, respectively, showing an increasing Raman shift from pure calcite to iron-bearing carbonates to magnesium-bearing carbonates as shown in Figure 2. This same progression was also visible in the subtler Raman peaks tabulated in Table 1. Raman active modes correspond to symmetry modes E<sub>g</sub> or A<sub>1g</sub>. The Raman peaks at ~1086 cm<sup>-1</sup> are attributed to the A<sub>1g</sub> stretching C-O mode. Raman peaks in the range of 700-900 cm<sup>-1</sup> correspond to bending modes of the carbonate ions with the low 700s peaks corresponding to in-plane deformation of the planar CO<sub>3</sub> units. Frequencies above 1000 cm<sup>-1</sup> correspond to the symmetrical single mode A<sub>1g</sub> and asymmetrical E<sub>g</sub> stretching *l* modes of the carbonate ion. The Raman peaks between 150 and 180 cm<sup>-1</sup> correspond to out-of-phase translations of the carbonate ions parallel to the (111) plane of the rhombohedral cell while the peaks in the 280s and low 300s correspond to in-phase librations of the carbonate ions around the twofold symmetry axes [38]. A<sub>#x</sub> symmetry modes correspond to nondegenerate single modes with only one set of atomic displacements. A *g* subscript refers to symmetric vibrations while a *u* subscript refers to antisymmetric vibrations. *Eg* symmetry modes involve two sets of atom displacements.

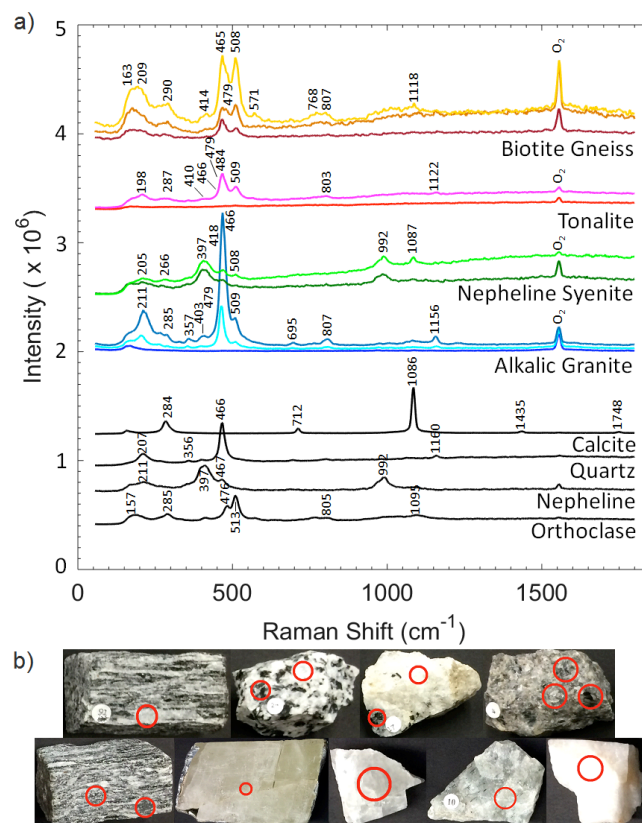


Fig 3. a) Biotite gneiss, tonalite, nepheline syenite, alkali granite, remote Raman spectra at a 5 m distance over 30 s integration time. Raman spectra of calcite, quartz, nepheline, and orthoclase are displayed for reference. Spectra were scaled and vertically shifted for viewing clarity. Biotite gneiss scaled x5 for bright spot, x10 for intermediate and dark spots. Nepheline syenite dark spot scaled x4. Tonalite and alkalic granite unscaled. Calcite scaled x0.2. Quartz scaled x2. Nepheline scaled

x8. Orthoclase scaled x2. b) Analyzed samples from left to right: Row 1: biotite gneiss light spot, tonalite, nepheline syenite, alkalic granite; Row 2: biotite gneiss intermediate and dark spot, calcite, quartz, nepheline, orthoclase. Laser target within red circle.

Figure 3 shows remote Raman spectra of light, dark, and roughly equal light and dark (banded) surface areas in biotite gneiss ( $K(Mg, Fe_{2+3})(Al, Fe^{3+})Si_3O_{10}(OH, F)_2$ ) and alkali granite, and light and dark colored areas in tonalite, and nepheline syenite ( $(Na,K)AlSiO_4$ ) at a 5 m standoff distance over a 30 s integration time. These measurement targets were chosen based on the surface grains visible to the naked eye, but do not represent the full internal crystal volume and resulting internal light penetration contribution to the Raman signal. Lighter areas have stronger Raman spectra for each sample group, darker areas have weaker spectra, and mixed areas have intermediate intensity spectra for each sample group.

For biotite gneiss, the lighter phases are made up of quartz and plagioclase mineral components as seen by the Raman peaks at 290, 414, 465, 479, 508, and 571  $cm^{-1}$ . These correlate with  $\alpha$ -quartz and the potassium feldspar orthoclase ( $KAlSi_3O_8$ ). Biotite peaks are visible at 287, 410, and the broad bands at 750-807  $cm^{-1}$  [23]. The lighter phases have a greater ratio of quartz to plagioclase feldspar while the mixed banded biotite gneiss has a slightly greater ratio of plagioclase to quartz. Both spectra exhibit moderately high levels of fast organic/bio-fluorescence background. The dark phases have no fast organic/bio-fluorescence background and favor a greater quartz over plagioclase feldspar ratio.

Alpha quartz typically produces a distinct Raman peak at 465  $cm^{-1}$  as a product of symmetric stretching of Si-O-Si. Smaller quartz modes between 200 and 400  $cm^{-1}$  correspond to lattice distortions. Plagioclase feldspars exhibit a doublet at  $\sim 475$ -510  $cm^{-1}$ . The observed 508  $cm^{-1}$  peak in biotite gneiss initially indicates the presence of low albite but further examination of the spectral shape and smaller Raman bands 768 and 807  $cm^{-1}$ , suggest an orthoclase K-feldspar interpretation (also confirmed by powder XRD analyses of the same rock). When the 475  $cm^{-1}$  peak is present alongside quartz, the 475  $cm^{-1}$  peak competes with the quartz 465  $cm^{-1}$  peak. This is a product of symmetric T-O-T stretching of the four-membered T-O<sub>4</sub> tetrahedral ring (T = Si or Al) [6], [23], [28], [39]. Variations in T-O-T bond angles determine the position of this Raman peak due to the motion of the oxygen atoms in the four-membered ring breathing mode perpendicular to the T-T line. The observed 571  $cm^{-1}$  peak is determined by the degree of Al-Si ordering [6], [28] and closely correlates with the orthoclase feldspar 568  $cm^{-1}$  peak. As demonstrated by the Raman spectra, the biotite gneiss sample has a combination of quartz, albite, orthoclase, and biotite.

The quartz phases found in our biotite gneiss sample are mostly white as compared to the darker plagioclase feldspar phases which appear light to dark grey. Biotite phases appear black. There are two interpretations for the unexpected quartz preference in the darker phases' quartz/plagioclase ratio: a) quartz has a more ordered and larger internal crystal volume than the plagioclase (or other) crystal volumes resulting in greater internal light penetration contributing to the Raman

signal, or b) a darker mafic mineral with weaker Raman signatures, such as biotite is intergrown with the plagioclase, making the plagioclase more opaque thus skewing the quartz/plagioclase ratio to prefer quartz. Overall spectral shape and broad Raman bands may indicate the presence of darker mafic minerals.

Light and dark spots were measured in tonalite (quartz diorite with a quartz content 5-20% of the rock) as shown in Figure 3. Moderate levels of fast organic/bio-fluorescence background are visible. Quartz Raman peaks are identified at 198, 466, and 803  $cm^{-1}$ . Plagioclase feldspar peaks are identified at 287, 484, 509, and 564  $cm^{-1}$  with a 479  $cm^{-1}$  feldspar peak and a 466  $cm^{-1}$  quartz peak as a shoulder of the 484  $cm^{-1}$  plagioclase peak [6], [23], [28], [39]. Intermediate plagioclase feldspars ranging from bytownite—oligoclase are represented by these Raman peaks, and possible K-feldspar microcline may be attributed to the 803 and 1122  $cm^{-1}$  peaks. The sample has a greater plagioclase to quartz component as demonstrated by the intensity of the plagioclase 479  $cm^{-1}$  and quartz 466  $cm^{-1}$  Raman peaks [6], [28]. Much broader regions at 700-850  $cm^{-1}$  and at 1050  $cm^{-1}$  are attributed to biotite [23]. Powder XRD measurements support the presence of intermediate plagioclase andesine, K-feldspar microcline, and quartz. Raman measurements additionally identify biotite.

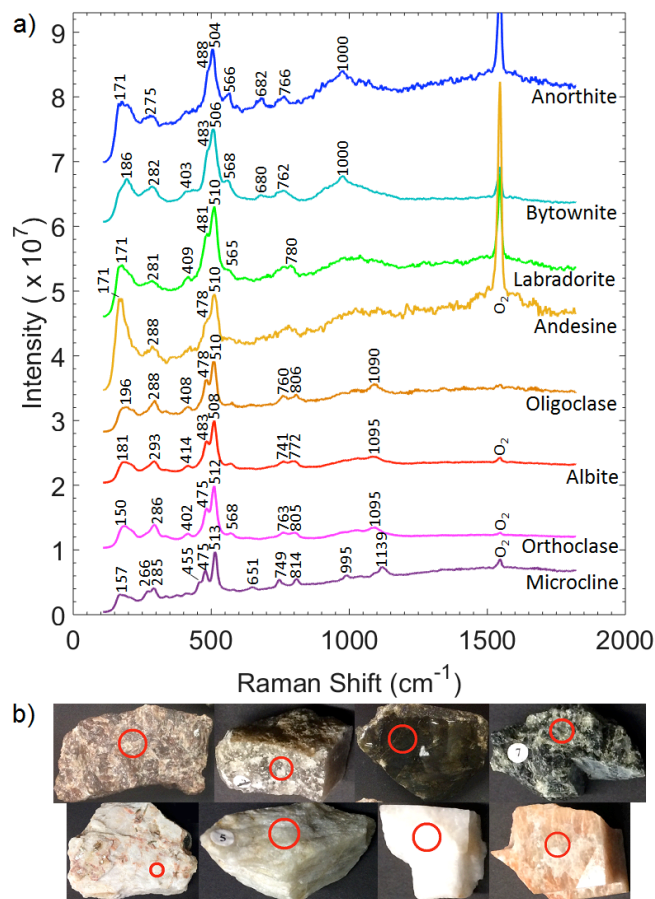


Fig 4. a) Remote Raman spectra of plagioclase and alkali feldspar solid series at a 5 m distance over a 30 s integration time. Spectra were scaled and vertically shifted for viewing clarity. Anorthite scaled x5.

Bytownite scaled x1.5. Labradorite scaled x4. Andesine scaled x10. Oligoclase scaled x1.1. Albite scaled x0.2. Orthoclase scaled x0.1. Microcline scaled x0.35. b) Analyzed samples from left to right: Row 1: anorthite, bytownite, labradorite, andesine; Row 2: oligoclase, albite, orthoclase, microcline. Laser target within red circle.

Light and dark spots were measured in nepheline syenite ((Na,K)AlSiO<sub>4</sub>) as shown in Figure 3. The sample exhibits moderately high levels of fast organic/bio-fluorescence background, particularly prominent in the lighter targets. Nepheline, plagioclase feldspar, quartz, and calcite are distinguishable in the nepheline syenite Raman spectrum. Nepheline in nepheline syenite is confirmed by the Raman peaks at 397 and 992 cm<sup>-1</sup> as verified through analyses of a pure nepheline sample. Only nepheline is readily identifiable in the dark target analyzed. Other mineral components identified in the lighter target were a calcite Raman peak attributed to the A<sub>1g</sub> stretching C-O mode at 1087 cm<sup>-1</sup> [38], an α-quartz peak at 467 cm<sup>-1</sup> product of symmetric stretching of Si-O-Si, a weaker α-quartz peak at 205 cm<sup>-1</sup> corresponding to lattice distortions [23], [39], and a low albite 508 cm<sup>-1</sup> peak product of corresponding T-O-T bond angles [6], [28]. Powder XRD measurements confirm the presence of nepheline, albite, and quartz. The lack of any K-feldspar detection indicates that the nepheline mineral component did not react with the quartz component during melt crystallization [40].

Figure 3 also shows alkalic granite remote Raman spectra of dark, light, and both light and dark spots with minimal to no fast organic/bio-fluorescence. Quartz is seen as a major component with Raman peaks at 211, 357, 466, and 1156 cm<sup>-1</sup>. Feldspar signatures are visible as 509, 268, 285, and 807 cm<sup>-1</sup> and the shifted quartz band from 465 to 466 cm<sup>-1</sup> supports the presence of feldspars. The 509 cm<sup>-1</sup> Raman peak indicates the presence of an intermediate plagioclase feldspar such as labradorite, andesine, or oligoclase, but the 268 and 285 cm<sup>-1</sup> doublet, the broad 1156 cm<sup>-1</sup> peak approaching 1139 cm<sup>-1</sup>, and the overall spectral shape in the region indicates the presence of microcline. Possible biotite peaks are visible at 403 cm<sup>-1</sup> and the broad bands at 750–800 cm<sup>-1</sup> [23]. Lighter phases are dominated by quartz and darker more opaque phases are dominated by feldspars or other mafic minerals in this alkali granite sample. Powder XRD measurements correlate with the Raman data indicating the presence of quartz and microcline, although biotite was not detected.

Figure 4 shows remote Raman spectra of the full plagioclase feldspars series (An<sub>0-100</sub>) and partial potassium feldspar series. Raman identification of albite (NaAlSi<sub>3</sub>O<sub>8</sub>), oligoclase (Na,Ca)(Al,Si)AlSi<sub>2</sub>O<sub>8</sub>, andesine (NaAlSi<sub>3</sub>O<sub>8</sub>-CaAl<sub>2</sub>Si<sub>2</sub>O<sub>8</sub>), labradorite (Ca,Na)Al(Al,Si)Si<sub>2</sub>O<sub>8</sub>, bytownite (NaSi,CaAl)AlSi<sub>2</sub>O<sub>8</sub>, and anorthite (CaAl<sub>2</sub>Si<sub>2</sub>O<sub>8</sub>) can be broadly classified into three groups: endmember anorthite, endmember albite, and intermediate plagioclases. Anorthite has a major peak at 504 cm<sup>-1</sup>. Albite has a major peak at 508 cm<sup>-1</sup> and 483 cm<sup>-1</sup>. The intermediate plagioclase feldspars have major peaks at 510 cm<sup>-1</sup> and 478–481 cm<sup>-1</sup>, with bytownite having a major peak at 506 cm<sup>-1</sup> and 483 cm<sup>-1</sup>. These peaks are a product of symmetric T-O-T stretching of the four-membered T-O<sub>4</sub> tetrahedral ring where T = Si or Al. The Raman peak at

293 cm<sup>-1</sup> (cage-shear modes) decreases with increasing anorthite content. The spectral shape of the single or double 760–830 cm<sup>-1</sup> peaks (deformation modes of tetrahedral) is useful as a diagnostic for identifying feldspars [6], [28], [41]. The peak at 1099 cm<sup>-1</sup> is characteristic of vas (Si-O-Al) antisymmetric stretching modes of framework silicates. These bands shift towards lower frequency with Al to Si substitutions [6], [41], [42]. A high level of background fluorescence is visible in the lighter phases, more consistent with sodium-rich albite or oligoclase while little to no background fluorescence is visible in the darker phases, more consistent with potassium-rich orthoclase. Internal reflections can contribute to a stronger fluorescence signal in lighter crystals [43] and absorption of photons can significantly reduce both Raman and fluorescence signals in the darker materials. For the partial potassium feldspar series: monoclinic orthoclase (KAlSi<sub>3</sub>O<sub>8</sub>) and triclinic microcline (KAlSi<sub>3</sub>O<sub>8</sub>), the major Raman peaks at 475–513 cm<sup>-1</sup> shift up with increasing crystal geometry.

Figure 5 shows remote Raman spectra of grey and red sandstone, quartz conglomerate, and quartzite. Organics in sedimentary rocks contribute to a fast fluorescence background observed in the four samples as the upward sloping fluorescence background towards the higher wavenumbers. This is consistent with biological detritus component of sandstones and other sedimentary rocks on Earth [44]. If the Martian surface materials are sterile, fast organic/bio-fluorescence should not be present [45]–[47]. Quartzite is displayed for comparison. It has a relatively flat baseline containing minimal to no fast organic/bio-fluorescence more typical of metamorphic rocks. Grey sandstone exhibits strong quartz and plagioclase Raman peaks at 212 and 468 cm<sup>-1</sup> and red sandstone exhibits both quartz and plagioclase peaks at 468 cm<sup>-1</sup> and 178 and 203 cm<sup>-1</sup> [6], [28]. Quartz conglomerate is visible with clear quartz peaks at 466 and 204 cm<sup>-1</sup>. Subtler broad bands at 513, 177, and 263 cm<sup>-1</sup> hint to K-feldspar components. Quartzite exhibits quartz Raman peaks at 465 and 205 cm<sup>-1</sup>.

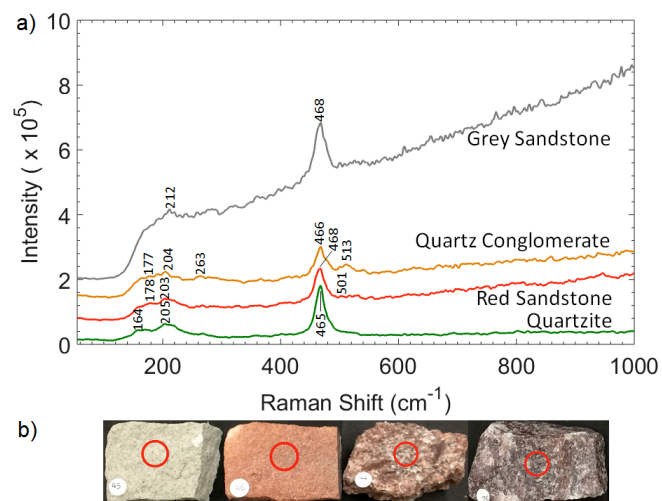


Fig 5. a) Grey sandstone, quartz conglomerate, red sandstone, and quartzite remote Raman spectra at a 5 m distance over 30 s integration time. Spectra were vertically shifted for viewing clarity. b) Analyzed

samples from left to right: grey sandstone, red sandstone, quartz conglomerate, quartzite. Laser target within red circle

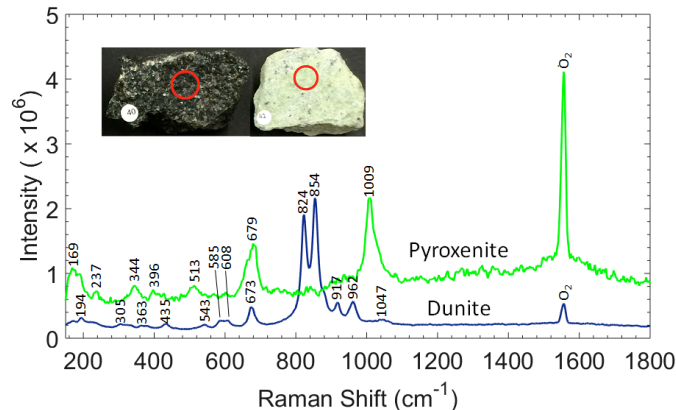


Fig. 6. Dunite and pyroxenite remote Raman spectra at a 5 m distance over a 120 s integration time. The main olivine peaks are visible at 824, and 854  $\text{cm}^{-1}$ . Pyroxene was scaled  $\times 10$  for viewing clarity. Photo insert: Analyzed samples from left to right: pyroxenite, dunite. Laser target within red circle.

Olivine-rich dunite ( $(\text{Mg,Fe})_2\text{SiO}_4$ ) and pyroxenite ( $(\text{Mg,Fe,Ca})_3\text{Si}_2\text{O}_6$ ) remote Raman spectra are shown in Figure 6. Olivine peaks are visible at 824, 854, 917, and 962  $\text{cm}^{-1}$ . The Raman spectra of olivines has a characteristic doublet between 808 and 825  $\text{cm}^{-1}$  as a result of  $\text{Si-O}_{\text{nb}}$  symmetric stretching band  $\text{A}_g(\text{Si-O})_{\text{s-str}}$ , and 837 and 858  $\text{cm}^{-1}$  as a result of  $\text{Si-O}_{\text{nb}}$  asymmetric stretching band  $\text{A}_g(\text{Si-O})_{\text{a-str}}$ . Dunite exhibits a doublet at 824  $\text{cm}^{-1}$  and 854  $\text{cm}^{-1}$  characteristic of forsterite [48], [49]. Chromite ( $\text{FeCr}_2\text{O}_4$ ) is visible at 673  $\text{cm}^{-1}$  [50]. Additional dunite peaks assigned are the  $\text{A}_g$  peaks at 194, 305, 543, and 962  $\text{cm}^{-1}$  product of  $\text{T}(\text{SiO}_4)$ , the  $\text{B}_{1g}+\text{B}_{2g}$  peak at 435  $\text{cm}^{-1}$ , and the  $\nu_3 \text{B}_{3g}$  peak at 917  $\text{cm}^{-1}$  [51]. Pyroxenite displays a harzburgite  $\nu_{16}$  peak at 1009  $\text{cm}^{-1}$  and a  $\nu_{11}$  peak at 679  $\text{cm}^{-1}$ . This peak is produced by the symmetric stretching vibration of Si-O bonds (where O is a non-bridging oxygen) in  $\text{SiO}_4$  tetrahedra [52]. These peak positions suggest iron enrichment concordant with the ultramafic nature of pyroxenites [53]. Additional minor peaks at 344 and 396  $\text{cm}^{-1}$  correspond to the  $\nu_3$  and  $\nu_4$  bands respectively. The peaks at 196 and 513  $\text{cm}^{-1}$  may be attributed to orthoclase or microcline but there are insufficient plagioclase peaks to establish a proper identity.

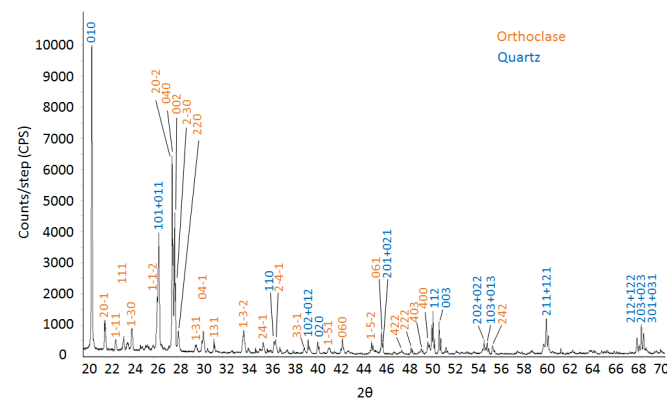


Fig. 7. Representative 10 minute XRD spectrum of a multiminerallitic natural rock confirms the presence of quartz and plagioclase in biotite gneiss sample. Major peaks have been labeled with corresponding lattice modes.

Similar to remote Raman, powder XRD measurements were capable of detecting major mineral components in multiminerallitic rocks. These measurements were useful in providing ground-truth data to support our remote Raman data. Figure 7 shows a powder XRD spectrum of biotite gneiss, confirming the presence of major rock components quartz and orthoclase. This XRD spectrum is representative of the quality of XRD data acquired for all of the samples in this study.

Raman spectral analysis of the plagioclase and potassium feldspars, biotite gneiss, tonalite, nepheline syenite, and alkalic granite demonstrate that remote Raman can easily detect end-member feldspars (albite, anorthite, microcline/orthoclase) in natural rocks. Intermediate feldspars and quartz, when found in natural rocks with complex mineralogies exhibit band shifts and broadening in the 504-510  $\text{cm}^{-1}$  and 600-1200  $\text{cm}^{-1}$  region. A good approximation of intermediate plagioclase feldspars is possible by using spectral shape and assigning other minor Raman peaks in addition to the 504-510  $\text{cm}^{-1}$  peaks. Remote Raman can also easily detect calcite, olivine, and pyroxene facilitating compositional characterization in multiminerallitic rocks. Lastly, despite strong organic/bio-fluorescence background, quartz and plagioclase were also identified in sedimentary rocks. Powder XRD analysis confirmed the mineral component identification determined from the remote Raman spectra. The lattice parameters are tabulated in Table 2.

## B. Planetary science applications

Remote Raman analysis on Mars or other rocky bodies will involve spectroscopic analysis in challenging environments with less than ideal sample conditions. Complex rock mineralogies, dusty conditions, and the presence of opaque mafic minerals, will introduce challenges to acquiring high quality remote Raman spectra. A first-order look at the remote Raman spectra of natural rocks with multiple mineral components provides an understanding of system capabilities, observed Raman peak positions, and the broader band shapes resulting from multiple overlapping Raman bands.

## 4. CONCLUSION

We have demonstrated the capabilities of a Compact Remote Raman+LIBS+Fluorescence System (CRRLFS) at a standoff distance of 5 m to analyze natural rocks in daylight conditions and with high fluorescence backgrounds, without sample preparation. Remote Raman spectra of natural multiminerallitic rocks results in Raman signal mixing from various phases and it is demonstrated that several mineral phases such as carbonates, quartz, feldspar, olivine, and pyroxene can be identified in rocks. The provided data and interpretation are necessary for accurate analysis of future Raman measurements on planetary surfaces such as on Mars, as expected from the NASA Mars 2020 rover mission. Expansion of the available published standoff Raman spectra of rocks with

complex mineralogies will aid in providing a more realistic assessment of the expected spectral data from these and other surface rover missions.

**Funding.** National Aeronautics and Space Administration (NASA) (NNX13AM98A); The SuperCam program under Mars 2020 mission.

**Acknowledgment.** The authors would like to thank: Mr. Mark Wood for writing the code to run the ICCD detector and the pulse generator and Dr. David Bates for developing custom software used to reduce and batch process Raman images into spectra.

## REFERENCES

- [1] C. K. Johnson, G. A. Dalickas, S. A. Payne, and R. M. Hochstrasser, "Picosecond timescale Raman processes and spectroscopy," *Pure Appl. Chem.*, vol. 57, no. 2, pp. 195–200, 1985.
- [2] I. R. Lewis and H. G. M. Edwards, *Handbook of Raman Spectroscopy: From the Research Laboratory to the Process Line*, 1st ed. New York: Marcel Dekker, 2001.
- [3] S. Maurice *et al.*, "The ChemCam instrument suite on the Mars Science Laboratory (MSL) rover: Science objectives and mast unit description," *Space Sci. Rev.*, vol. 170, no. 1–4, pp. 95–166, 2012.
- [4] R. C. Wiens, S. K. Sharma, J. Thompson, A. Misra, and P. G. Lucey, "Joint analyses by laser-induced breakdown spectroscopy (LIBS) and Raman spectroscopy at stand-off distances," *Spectrochim. Acta - Part A Mol. Biomol. Spectrosc.*, vol. 61, no. 10, pp. 2324–2334, 2005.
- [5] J. Mustard *et al.*, "Report of the Mars 2020 Science Definition Team," *Mars Explor. Progr. Anal. Gr.*, no. C1, pp. 155–205, 2013.
- [6] S. K. Sharma, S. M. Angel, M. Ghosh, H. W. Hubble, and P. G. Lucey, "Remote pulsed laser Raman spectroscopy system for mineral analysis on planetary surfaces to 66 meters," *Appl. Spectrosc.*, vol. 56, no. 6, pp. 699–705, 2002.
- [7] S. K. Sharma, "New trends in telescopic remote Raman spectroscopic instrumentation," *Spectrochim. Acta - Part A Mol. Biomol. Spectrosc.*, vol. 68, no. 4, pp. 1008–1022, 2007.
- [8] J. Jehlička, P. Vitek, H. G. M. Edwards, M. Heagraves, and T. Čapoun, "Application of portable Raman instruments for fast and non-destructive detection of minerals on outcrops," *Spectrochim. Acta - Part A Mol. Biomol. Spectrosc.*, vol. 73, no. 3, pp. 410–419, 2009.
- [9] F. Rull, A. Vegas, A. Sansano, and P. Sobron, "Analysis of Arctic ices by Remote Raman Spectroscopy," *Spectrochim. Acta - Part A Mol. Biomol. Spectrosc.*, vol. 80, no. 1, pp. 148–155, 2011.
- [10] S. M. Angel, N. R. Gomer, S. K. Sharma, C. McKay, and N. Ames, "Remote Raman spectroscopy for planetary exploration: A review," *Appl. Spectrosc.*, vol. 66, no. 2, pp. 137–150, 2012.
- [11] P. J. Gasda, T. E. Acosta-Maeda, P. G. Lucey, A. K. Misra, S. K. Sharma, and G. J. Taylor, "Next generation laser-based standoff spectroscopy techniques for Mars exploration," *Appl. Spectrosc.*, vol. 69, no. 2, pp. 173–192, 2015.
- [12] R. C. Wiens *et al.*, "THE SUPERCAM REMOTE RAMAN SPECTROMETER FOR MARS 2020," *LPSC XLVIII*, no. Abstract #2600, 2017.
- [13] N. Tarcea *et al.*, "Raman Spectroscopy—A Powerful Tool for in situ Planetary Science," *Space Sci. Rev.*, vol. 135, no. 1–4, pp. 281–292, Mar. 2008.
- [14] V. Klein *et al.*, "Remote Raman spectroscopy as a prospective tool for planetary surfaces," *J. Raman Spectrosc.*, vol. 35, no. 6, pp. 433–440, Jun. 2004.
- [15] P. Colomban, "The on-site/remote Raman analysis with mobile instruments: a review of drawbacks and success in cultural heritage studies and other associated fields," *J. Raman Spectrosc.*, vol. 43, no. 11, pp. 1529–1535, Nov. 2012.
- [16] J. Blacksberg, G. R. Rossman, and A. Gleckler, "Time-resolved Raman spectroscopy for in situ planetary mineralogy," *Appl. Opt.*, vol. 49, no. 26, pp. 4951–4962, 2010.
- [17] A. K. Misra, S. K. Sharma, P. G. Lucey, R. C. F. Lentz, and C. H. Chio, "Daytime rapid detection of minerals and organics from 50 and 100 m distances using a Remote Raman system," *Lidar Remote Sens. Environ. Monit. VIII*, vol. 6681, no. 2007, p. 66810C–66810C–14, 2007.
- [18] T. E. Acosta-Maeda *et al.*, "Remote Raman measurements of minerals, organics, and inorganics at 430 m range," *Appl. Opt.*, vol. 55, no. 36, p. 10283, 2016.
- [19] A. K. Misra, S. K. Sharma, and P. G. Lucey, "Remote Raman spectroscopic detection of minerals and organics under illuminated conditions from a distance of 10 m using a single 532 nm laser pulse," *Appl. Spectrosc.*, vol. 60, no. 2, pp. 223–228, 2006.
- [20] S. K. Sharma, A. K. Misra, S. M. Clegg, J. E. Barefield, R. C. Wiens, and T. Acosta, "Time-resolved remote Raman study of minerals under supercritical CO<sub>2</sub> and high temperatures relevant to Venus exploration," *Philos. Trans. A. Math. Phys. Eng. Sci.*, vol. 368, no. 1922, pp. 3167–3191, 2010.
- [21] S. K. Sharma *et al.*, "Remote-Raman spectroscopic study of minerals under supercritical CO<sub>2</sub> relevant to Venus exploration," *Spectrochim. Acta - Part A Mol. Biomol. Spectrosc.*, vol. 80, no. 1, pp. 75–81, 2011.
- [22] J. D. Stopar, P. G. Lucey, S. K. Sharma, A. K. Misra, and H. W. Hubble, "A remote Raman system for planetary exploration: Evaluating remote Raman efficiency," *Instruments, Methods, Mission. Astrobiol. VII*, vol. 5163, pp. 99–110, 2004.
- [23] J. D. Stopar, P. G. Lucey, S. K. Sharma, A. K. Misra, G. J. Taylor, and H. W. Hubble, "Raman efficiencies of natural rocks and minerals: Performance of a remote Raman system for planetary exploration at a distance of 10 meters," *Spectrochim. Acta - Part A Mol. Biomol. Spectrosc.*, vol. 61, no. 10, pp. 2315–2323, 2005.
- [24] S. K. Sharma, A. K. Misra, P. G. Lucey, and R. C. F. Lentz, "A combined remote Raman and LIBS instrument for characterizing minerals with 532 nm laser excitation," *Spectrochim. Acta - Part A Mol. Biomol. Spectrosc.*, vol. 73, no. 3, pp. 468–476, 2009.
- [25] A. K. Misra, S. K. Sharma, T. E. Acosta, J. N. Porter, and D. E. Bates, "Single-pulse standoff Raman detection of chemicals from 120 m distance during daytime," *Appl. Spectrosc.*, vol. 66, no. 11, pp. 1279–1285, 2012.

- [26] A. Wang *et al.*, "Development of the Mars microbeam Raman spectrometer (MMRS)," *J. Geophys. Res.*, vol. 108, no. E1, p. 5005, 2003.
- [27] G. Bazalgette Courrèges-Lacoste, B. Ahlers, and F. R. Pérez, "Combined Raman spectrometer/laser-induced breakdown spectrometer for the next ESA mission to Mars," *Spectrochim. Acta - Part A Mol. Biomol. Spectrosc.*, vol. 68, no. 4, pp. 1023–1028, 2007.
- [28] J. J. Freeman, A. Wang, K. E. Kuebler, B. L. Jolliff, and L. A. Haskin, "Characterization of natural feldspars by raman spectroscopy for future planetary exploration," *Can. Mineral.*, vol. 46, no. 6, pp. 1477–1500, 2008.
- [29] L. a. Haskin, A. Wang, K. M. Rockow, B. L. Jolliff, R. L. Korotev, and K. M. Viskupic, "Raman spectroscopy for mineral identification and quantification for in situ planetary surface analysis : A point count method," *J. Geophys. Res.*, vol. 102, no. 97, pp. 19293–19306, 1997.
- [30] I. Martínez-Arkarazo, D. C. Smith, O. Zuloaga, M. A. Olazabal, and J. M. Madariaga, "Evaluation of three different mobile Raman microscopes employed to study deteriorated civil building stones," *J. Raman Spectrosc.*, vol. 39, no. 8, pp. 1018–1029, Aug. 2008.
- [31] J. Moros, J. A. Lorenzo, P. Lucena, L. M. Tobaría, and J. Laserna, "Simultaneous Raman Spectroscopy - Laser-Induced Breakdown Spectroscopy for Instant Standoff Analysis of Explosives Using a Mobile Integrated Sensor Platform," vol. 82, no. 4, pp. 1389–1400, 2010.
- [32] B. Zachhuber, G. Ramer, A. Hobro, E. t. H. Chrysostom, and B. Lendl, "Stand-off Raman spectroscopy: a powerful technique for qualitative and quantitative analysis of inorganic and organic compounds including explosives," *Anal. Bioanal. Chem.*, vol. 400, no. 8, pp. 2439–2447, Jun. 2011.
- [33] Q. Lin, G. Niu, Q. Wang, Q. Yu, and Y. Duan, "Combined Laser-Induced Breakdown with Raman Spectroscopy : Historical Technology Development and Recent Applications Combined Laser-Induced Breakdown with Raman Spectroscopy : Historical Technology Development," *Appl. Spectrosc. Rev.*, vol. 48:6, no. June 2017, pp. 487–508, 2013.
- [34] C. S. Garcia *et al.*, "Remote Raman sensor system for testing of rocks and minerals," *Proc. SPIE*, vol. 6538, p. 65381I–65381I–9, 2007.
- [35] S. K. Sharma, P. G. Lucey, M. Ghosh, H. W. Hubble, and K. A. Horton, "Stand-off Raman spectroscopic detection of minerals on planetary surfaces," *Spectrochim. Acta - Part A Mol. Biomol. Spectrosc.*, vol. 59, no. 10, pp. 2391–2407, 2003.
- [36] A. K. Misra, S. K. Sharma, C. H. Chio, P. G. Lucey, and B. Lienert, "Pulsed remote Raman system for daytime measurements of mineral spectra," *Spectrochim. Acta - Part A Mol. Biomol. Spectrosc.*, vol. 61, no. 10, pp. 2281–2287, 2005.
- [37] A. K. Misra, S. K. Sharma, T. E. Acosta, and D. E. Bates, "Compact remote Raman and LIBS system for detection of minerals, water, ices and atmospheric gases for planetary exploration," *Proc. SPIE - Int. Soc. Opt. Eng.*, vol. 8032, no. 2, p. 80320Q–80320Q–12, 2011.
- [38] M. Prencipe, F. Pascale, C. M. Zicovich-Wilson, V. R. Saunders, R. Orlando, and R. Dovesi, "The vibrational spectrum of calcite (CaCO<sub>3</sub>): An ab initio quantum-mechanical calculation," *Phys. Chem. Miner.*, vol. 31, no. 8, pp. 559–564, 2004.
- [39] C. H. Chio, S. K. Sharma, P. G. Lucey, and D. W. Muenow, "Effects of particle size and laser-induced heating on the Raman spectra of alpha quartz grains," *Appl. Spectrosc.*, vol. 57, no. 7, pp. 774–783, 2003.
- [40] T. A. Rickard, "The Cripple Creek Volcano," *Trans. the American Inst. Min. Eng.*, vol. XXX, pp. 367–403, 1901.
- [41] S. K. Sharma, J. A. Philpotts, and D. W. Matson, "Ring distributions in alkali- and alkaline-earth aluminosilicate framework glasses- a raman spectroscopic study," *J. Non. Cryst. Solids*, vol. 71, no. 1–3, pp. 403–410, May 1985.
- [42] D. W. Matson, S. K. Sharma, and J. A. Philpotts, "Raman spectra of some tectosilicates and of glasses along the orthoclase-anorthite and nepheline-anorthite joins," *Am. Mineral.*, vol. 71, pp. 694–704, 1986.
- [43] B. J. Bozlee, A. K. Misra, S. K. Sharma, and M. Ingram, "Remote Raman and fluorescence studies of mineral samples," *Spectrochim. Acta - Part A Mol. Biomol. Spectrosc.*, vol. 61, no. 10, pp. 2342–2348, 2005.
- [44] A. K. Misra *et al.*, "'Standoff Biofinder' for fast, noncontact, nondestructive, large-area detection of biological materials for planetary exploration," *Astrobiology*, vol. 16, no. 9, pp. 715–729, 2016.
- [45] A. Ellery, D. Wynn-Williams, J. Parnell, H. G. M. Edwards, and D. Dickensheets, "The role of Raman spectroscopy as an astrobiological tool in the exploration of Mars," *J. Raman Spectrosc.*, vol. 35, no. 6, pp. 441–457, Jun. 2004.
- [46] J. Popp and M. Schmitt, "Raman spectroscopy breaking terrestrial barriers!," *J. Raman Spectrosc.*, vol. 35, no. 6, pp. 429–432, Jun. 2004.
- [47] I. B. Hutchinson *et al.*, "Raman spectroscopy on Mars: identification of geological and bio-geological signatures in Martian analogues using miniaturized Raman spectrometers," *Philos. Trans. R. Soc., A*, vol. 372, p. 20140204, 2014.
- [48] T. Mouri and M. Enami, "Raman spectroscopic study of olivine-group minerals," *J. Mineral. Petrol. Sci.*, vol. 103, pp. 100–104, 2008.
- [49] S. Y. Wang, S. K. Sharma, and T. F. Cooney, "Micro-Raman and infrared spectral study of forsterite under high pressure," *Am. Mi*, vol. 78, pp. 469–476, 1993.
- [50] B. Lafuente, R. T. Downs, H. Yang, and N. Stone, *The power of databases: the RRUFF project*. Berlin, Germany: W. De Gruyter, 2015.
- [51] B. A. Kolesov and C. A. Geiger, "A Raman spectroscopic study of Fe-Mg olivines," *Phys. Chem. Miner.*, vol. 31, no. 3, pp. 142–154, 2004.
- [52] A. Wang, B. L. Jolliff, and L. A. Haskin, "Raman spectroscopic characterization of a highly weathered basalt: Igneous mineralogy, alteration products, and a microorganism," *J. Geophys. Res.*, vol. 104, no. E11, pp. 27067–27077, 1999.
- [53] E. Huang, C. H. Chen, T. Huang, E. H. Lin, and J. A. Xu, "Raman spectroscopic characteristics of Mg-Fe-Ca pyroxenes," *Am. Mineral.*, vol. 85, no. 3–4, pp. 473–479, 2000.

Rock	Biotite Gneiss	Tonalite	Nepheline Syenite	Alkalic Granite	Grey Sandstone	Quartz Conglomerate	Red Sandstone	Quartzite	Pyroxenite (Ca,Na)(Mg,Fe, Al,Ti)(Si,Al) <sub>2</sub> O <sub>6</sub>	Dunite (Mg, Fe) <sub>2</sub> SiO <sub>4</sub>	Orthoclase KAlSi <sub>3</sub> O <sub>8</sub>	Microcline KAlSi <sub>3</sub> O <sub>8</sub>
Formula			(Na,K)AlSiO <sub>4</sub>					SiO <sub>2</sub>				
a (Angstroms)	4.932964	8.238786	10.015234	4.934592	4.923886	4.9347	4.921953	4.921711	18.306443	4.778417	8.176266	8.594629
+/-	0.002056	0.030751	0.003734	0.004428	0.001506	0.002585	0.000608	0.000593	0.01261	0.001952	0.003758	0.008305
b	4.932964	12.93273	10.015234	4.934592	4.923886	4.9347	4.921953	4.921711	8.85674	10.251157	12.848525	13.010332
+/-		0.034301							0.006255	0.004036	0.003558	0.007579
c	5.416536	7.135026	8.395675	5.414761	5.415882	5.420842	5.414617	5.414345	5.201067	6.010546	7.158585	7.243452
+/-	0.003991	0.021366	0.004152	0.007331	0.002458	0.004277	0.000993	0.001054	0.00414	0.003385	0.003171	0.006952
α (degrees)	90	93.50588	90	90	90	90	90	90	90	90	94.08863	90.66313
+/-		0.24843									0.03139	0.05989
θ	90	116.15785	90	90	90	90	90	90	90	90	116.53464	115.98662
+/-		0.27119									0.03691	0.07846
γ	120	90.40357	120	120	120	120	120	120	90	90	88.66065	87.82668
+/-		0.26573									0.03147	0.06619
v (Angstroms ^3)	114.147955	680.608055	729.303758	114.185882	113.714485	114.319145	113.598685	113.5818	843.277033	294.422418	671.07228	727.530862
+/-	0.214507	3.438308	0.552725	0.420399	0.141633	0.245398	0.057167	0.058497	1.176014	0.355498	0.424394	0.984828

Rock	Albite	Oligoclase	Andesine	Labradorite	Bytownite	Anorthite	Calcite	Pink Marble	Dolomite	Siderite	Milky Quartz
Formula	NaAlSi <sub>3</sub> O <sub>8</sub>	(Na,Ca)Al <sub>1-2</sub> Si <sub>3</sub> O <sub>8</sub>	(Na,Ca)Al <sub>1-2</sub> Si <sub>3</sub> O <sub>8</sub>	(Na,Ca) <sub>1-2</sub> Si <sub>3-2</sub> O <sub>8</sub>	(Ca,Na)Al <sub>1-2</sub> Si <sub>3</sub> O <sub>8</sub>	CaAl <sub>2</sub> Si <sub>2</sub> O <sub>8</sub>	CaCO <sub>3</sub>	(CaFe(CO <sub>3</sub> ) <sub>2</sub> )	(CaMg(CO <sub>3</sub> ) <sub>2</sub> )	FeCO <sub>3</sub>	SiO <sub>2</sub>
a (Angstroms)	8.174288	8.183378	8.198722	8.173481	8.189075	8.204633	4.99529	4.990455	4.819775	4.819226	4.92046
+/-	0.006502	0.004023	0.013243	0.009483	0.013925	0.011269	0.000483	0.001315	0.002231	0.001739	0.002621
b	12.873671	12.85317	12.908695	12.91306	12.895838	12.916101	4.99529	4.990455	4.819775	4.819226	4.92046
+/-	0.00614	0.004683	0.010414	0.010829	0.014	0.018276					
c	7.141906	7.157863	7.138143	7.131378	7.138364	14.225405	17.076196	17.055217	16.096948	16.088341	5.417164
+/-	0.005419	0.003595	0.009708	0.009171	0.024029	0.019931	0.002334	0.00635	0.010657	0.0083	0.004543
α (degrees)	93.8283	93.89555	93.62795	93.6674	93.46702	93.16938	90	90	90	90	90
+/-	0.05912	0.03665	0.10459	0.09323	0.1238	0.10869					
θ	116.4035	116.47677	116.13475	116.3499	115.9255	116.00778	90	90	90	90	90
+/-	0.0645	0.04331	0.12113	0.1022	0.14468	0.113					
γ	89.1156	88.83956	89.63235	89.70035	90.61581	91.02879	120	120	120	120	120
+/-	0.05726	0.03524	0.11092	0.08732	0.14566	0.10002					
v (Angstroms ^3)	671.577502	672.3159	676.672587	672.8682	1343.503918	1351.266994	369.014277	367.847807	323.837955	323.590975	113.583159
+/-	0.729901	0.48076	1.391916	1.178401	3.209779	3.049604	0.114779	0.312085	0.505758	0.393943	0.254842

Table 2: Powder XRD diffraction crystal lattice parameters.